

The Star Formation History in The Far Outer Disc of M33

Michael K. Barker^{1*}, A. M. N. Ferguson^{1†}, A. A. Cole², R. Ibata³, M. Irwin⁴,
G. F. Lewis⁵, T. A. Smecker-Hane⁶, N. R. Tanvir⁷

¹*Institute for Astronomy, University of Edinburgh, Blackford Hill, Edinburgh, UK, EH9 3HJ,*

²*School of Mathematics & Physics, University of Tasmania, Private Bag 37, Hobart, 7001, TAS, Australia,*

³*Observatoire Astronomique de Strasbourg, Strasbourg, France,*

⁴*Institute of Astronomy, Cambridge University, Cambridge, UK,*

⁵*Sydney Institute of Astronomy, School of Physics, The University of Sydney, NSW 2006, Australia*

⁶*Department of Physics & Astronomy, University of California, Irvine, USA*

⁷*Department of Physics and Astronomy, University of Leicester, Leicester, UK*

Accepted —. Received —; in original form —

ABSTRACT

The outer regions of disc galaxies are becoming increasingly recognized as key testing sites for models of disc assembly and evolution. Important issues are the epoch at which the bulk of the stars in these regions formed and how discs grow radially over time. To address these issues, we use *Hubble Space Telescope* Advanced Camera for Surveys imaging to study the star formation history (SFH) of two fields at 9.1 and 11.6 kpc along M33's northern major axis. These fields lie at ~ 4 and 5 V -band disc scale-lengths and straddle the break in M33's surface brightness profile. The colour-magnitude diagrams (CMDs) reach the ancient main sequence turnoff with a signal-to-noise ratio of ~ 5 . From detailed modelling of the CMDs, we find that the majority of stars in both fields combined formed at $z < 1$. The mean age in the inner field, S1, is $\sim 3 \pm 1$ Gyr and the mean metallicity is $[M/H] \sim -0.5 \pm 0.2$ dex. The star formation history of S1 unambiguously reveals how the inside-out growth previously measured for M33's inner disc out to ~ 6 kpc extends out to the disc edge at ~ 9 kpc. In comparison, the outer field, S2, is older (mean age $\sim 7 \pm 2$ Gyr), more metal-poor (mean $[M/H] \sim -0.8 \pm 0.3$ dex), and contains ~ 30 times less stellar mass. These results provide the most compelling evidence yet that M33's age gradient reverses at large radii near the disc break and that this reversal is accompanied by a break in stellar mass surface density. We discuss several possible interpretations of this behaviour including radial stellar mixing, warping of the gaseous disc, a change in star formation efficiency, and a transition to another structural component. These results offer one of the most detailed views yet of the peripheral regions of any disc galaxy and provide a much-needed observational constraint on the last major epoch of star formation in the outer disc.

Key words: galaxies: abundances, galaxies: evolution, galaxies: individual: Messier Number: M33, galaxies: stellar content, galaxies: spiral, galaxies: Local Group

1 INTRODUCTION

The traditional theory of disc galaxy formation holds that isolated discs form through the dissipational collapse of gaseous protogalaxies embedded in cold dark matter (CDM) haloes (White & Rees 1978; Fall & Efstathiou 1980; Peebles 1984). N-body/SPH simulations of structure formation in a CDM Universe have shown the importance of the cosmological context to disc formation, as galaxies grow through the

hierarchical merging and accretion of many smaller systems and through the inflow of intergalactic gas (e.g. Steinmetz & Navarro 2002; Abadi et al. 2003; Sommer-Larsen et al. 2003; Governato et al. 2009). The relative proportion of these two growth mechanisms through time may have a large effect on a galaxy's morphology today, as gas accretion tends to build thin discs and merging tends to build spheroids and thick discs (Steinmetz & Navarro 2002; Brook et al. 2004; Brooks et al. 2009). Other works have stressed the importance of gas-rich major mergers as an alternate or complementary disc formation channel to the ones above (Robertson et al.

* mkb@roe.ac.uk

† ferguson@roe.ac.uk

2006; Stewart et al. 2009). In reality, all of these mechanisms may operate at different levels depending on a galaxy’s environment (Blanton et al. 2003) and may contribute to diverse properties of outer discs and haloes.

Simulations of disc galaxies in a cosmological context have advanced to the point where they can make detailed predictions for their assembly history and observable internal properties. A common prediction is that present-day thin discs formed the bulk of their stars relatively late, at $z \lesssim 1$, because the major merger rate at earlier epochs was too high for any pre-existing thin disc to survive (Abadi et al. 2003; Sommer-Larsen et al. 2003; Governato et al. 2009). While there is still uncertainty in their sub-grid physical models of star formation, stellar feedback, and the multi-phase ISM (e.g. Okamoto et al. 2005), the simulations agree that stellar ages and chemical compositions contain clues to the formation and evolution of spiral galaxies. Therefore, spatially-resolved observational estimates of the star formation histories (SFHs) within spirals can provide powerful constraints on the simulations and their sub-grid physical models. These constraints are more robust against degeneracies when they come from colour-magnitude diagrams (CMDs) of resolved stars than when they rely on integrated, unresolved starlight. Some progress in this area has been made using the Advanced Camera for Surveys (ACS) aboard the *Hubble Space Telescope* to observe galaxies in the Local Group (LG) and nearby Universe (Brown et al. 2006; Williams et al. 2009a). However, the small field-of-view of ACS often makes it unclear which galactic component, or mix of components has been imaged (thin disc, thick disc, bulge, halo, accreted substructure, disturbed disc, etc.). This problem is particularly acute in MW-type spirals, which have non-negligible bulges and are more likely to have experienced massive satellite accretion, which can hinder efforts to study purely dissipative disc formation and secular evolution.

The late-type LG spiral, M33, potentially offers a clearer view of disc evolution than M31 or the MW because it has little or no bulge component (Bothun 1992; Minniti et al. 1993; McLean & Liu 1996). Such bulgeless disc galaxies are common in the Universe and the most challenging to produce in cosmological simulations, so a better observational determination of their evolution provides a rigorous benchmark for our understanding of disc formation (Mayer et al. 2008; Kautsch 2009). M33 is also interesting because it is one of a class of galaxies that exhibit truncations in their radial surface brightness (SB) profiles (Pohlen & Trujillo 2006; Ferguson et al. 2007). What causes these truncations is unclear, but they could arise naturally from the collapse of a uniformly-rotating, homogeneous protogalactic gas cloud under angular momentum conservation (van der Kruit 1987), or they could be related to star formation thresholds (Elmegreen & Parravano 1994; van den Bosch 2001; Schaye 2004). In M33, the break radius in the azimuthally averaged SB profile lies at $\sim 36'$ (Ferguson et al. 2007) and the V -band inner disc scale-length is $\sim 9.2'$ (Guidoni et al. 1981). The optical radius is $R_{25} = 35.4'$, defined as the radius at which the B-band SB is $25.0 \text{ mag arcsec}^{-2}$ (de Vaucouleurs et al. 1991).

Using CMDs of resolved stars in M33, Barker et al. (2007, hereafter B07) found a positive age gradient in three ACS fields just outside the break radius on the southern mi-

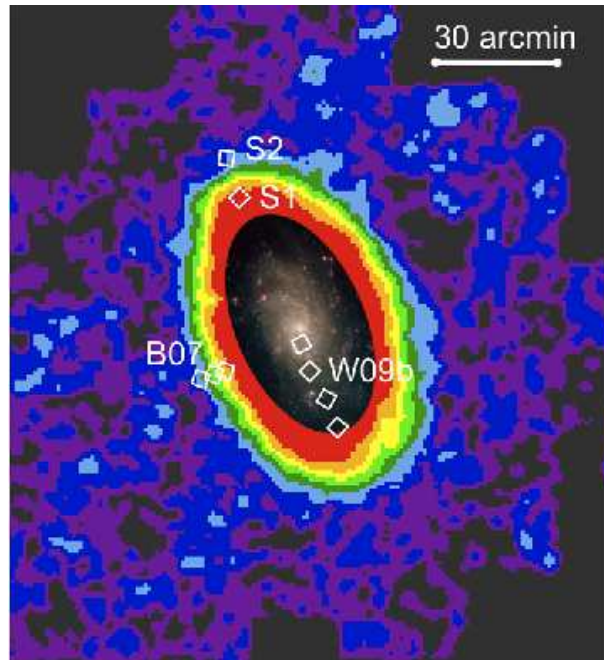


Figure 1. Contour map of M33 RGB stars from the INT/WFC survey with an optical image of the inner disc overlaid. The coloured contours represent equal logarithmic intervals of RGB stellar surface density. The ACS fields studied in this paper are labelled S1 and S2. The fields studied by B07 and W09b lie on the southern minor and major axes, respectively. The legend in the upper right corner shows the scale of $30'$.

nor axis. More recently, Williams et al. (2009b, hereafter W09b) found a negative age gradient in four ACS fields within the break radius on M33’s southern major axis. W09b argued that these seemingly contradictory results could be reconciled by the simulation of Roškar et al. (2008b), in which the inner disc of a spiral galaxy forms inside-out, but secular processes radially redistribute stars causing an inflection point in the stellar age gradient at the break radius.

Some open questions remain, however, since the B07 and W09b fields sample a small fraction of M33 and lie at different position angles. As shown by McConnachie et al. (2006) from spectroscopy of red giant branch (RGB) stars and by Sarajedini et al. (2006) from the periods of RR Lyrae stars, M33 hosts a metal-poor field halo population. McConnachie et al. (2006) also found three kinematic components on the southern major axis including a dominant disc, minority halo, and a third component which they attributed to a possible tidal stream. More recently, McConnachie et al. (2009) uncovered two giant tidal tails extending from the northern and southern disc regions. Hence, it is important to measure the SFH at as many different locations as possible to better understand and disentangle the contributions of different structural components and to safeguard against spatial variations within any one component.

In this paper, we examine the stellar populations in two ACS fields located at $36'$ and $46'$ along M33’s northern major axis. The fields lie at ~ 4 and 5 V -band scale-lengths, or 9.1 and 11.6 kpc, assuming a distance of 867 kpc (Galietti et al. 2004), inclination of 56° and position angle of 23° (Corbelli & Schneider 1997). Fig. 1 shows the locations of

these fields, and those studied by B07 and W09b, on a contour map of RGB stars from the Isaac Newton Telescope Wide Field Camera (INT/WFC) survey of M33 (Ferguson et al. 2007). The contours represent equal logarithmic intervals of RGB stellar surface density. Overlaid on the RGB map is an optical image of the inner disc on the same spatial scale. Our two fields, henceforth called S1 and S2, straddle the break in M33’s SB profile and provide one of the deepest views yet of the stellar populations in the outskirts of a disc galaxy.

In the next section, we describe the observations and data reduction and in §3, we examine the CMDs. We outline in §4.1 our method for fitting the CMDs to obtain the SFH. In §4.2, we present the results of the CMD fitting analysis and in §5, we discuss the implications. Finally, we summarise our results in §6.

2 OBSERVATIONS

The observations of S1 and S2 were made in June 2004 and August 2004, respectively, for Program ID 9837 (PI: Ferguson). The coordinates were $(\alpha_{J2000}, \delta_{J2000}) = (01^h 34^m 58.8^s, +31^\circ 12' 00.0'')$ for S1 and $(01^h 35^m 15.0^s, +31^\circ 22' 00.0'')$ for S2. Each field was observed over a period of 12 orbits using the F606W (broad V_J) and F814W ($\sim I_c$) filters. To facilitate removal of cosmic rays and bad pixels, 8 dithered sub-exposures totaling 10350s were taken in F606W and 16 sub-exposures totaling 20700s were taken in F814W. We photometered the images using the ACS module of the DOLPHOT software package¹. DOLPHOT takes as input the individual flat-fielded, dark-subtracted FLT images produced by the CALACS pipeline in addition to a reference image used for a common pixel coordinate system. We selected the deepest F814W DRZ image automatically produced by the pipeline to use as a reference, which was corrected for geometric distortion. We used the recommended values of input parameters listed in the DOLPHOT manual except we turned off the option to do a second pass of star finding and photometry because this increased the scatter in the CMD. DOLPHOT performs PSF-fitting photometry using a library of precomputed TinyTim PSFs, applies charge transfer efficiency corrections (Riess & Mack 2004), and reports final magnitudes in the VEGAMAG and Johnson-Cousins system using the zero-points and transformations in Sirianni et al. (2005).

To minimize contamination from non-stellar and poorly-measured objects in the final photometric catalogs, we required sources to have signal-to-noise ratio > 5 in both filters, $|F606W_{sharp} + F814W_{sharp}| \leq 0.3$, $(F606W_{crowd} + F814W_{crowd}) \leq 0.1$, error flag ≤ 7 in both filters, and overall object type ≤ 2 . The sharpness parameter measures the sharpness of sources; good stars have values close to zero while extended objects and incompletely masked cosmic rays tend to have large negative and positive values, respectively. The crowding parameter tells by how many magnitudes brighter a star would have been recovered had

nearby stars not been fit simultaneously. Large values suggest that a star’s magnitude was seriously affected by neighbors. We settled on thresholds for these parameters that produced clean CMDs and the best possible fits to the CMDs. Additionally, an error flag > 7 indicates an extreme case of saturation or that too much of the photometry aperture extends off a chip edge, and objects with type > 2 are too sharp, extended, or elongated. Fig. 2 shows the CMDs for the final catalogs, which contain 72068 and 2304 sources in S1 and S2, respectively. The contours in the left-hand panel of Fig. 2 correspond to stellar densities of $[1.0, 1.5, 2.25, 3.4, 5.1, 7.65, 11.5] \times 10^4 \text{ mag}^{-2}$. The drastic difference in stellar density between the fields despite their being located only ~ 1 V-band scale-length apart is due to the fact that they bracket M33’s break radius.

Artificial star tests were performed in the standard way to assess photometric errors and completeness. Roughly 3.5×10^6 artificial stars were injected uniformly on the images with magnitudes and colours populating the entire CMD and they were measured in exactly the same way as the real stars. The error bars on the right side of each panel in Fig. 2 show the median photometric errors (i.e., the difference between input and recovered colours and magnitudes) derived from the artificial star tests. The median F814W error reaches 0.1 mag at $F814W \sim 27.1$ (27.8) in S1 (S2) and the median colour error reaches 0.1 mag at $F814W \sim 27.6$ (27.4) in S1 (S2). The colour error reaches 0.1 mag at a fainter magnitude than the F814W error in S1 because the errors in the two filters are strongly correlated. This correlation is insignificant in S2 because S2 has a much lower level of crowding. The completeness curves are plotted on the CMDs in Fig. 2. The artificial star tests indicate that 50% completeness occurs at $F814W \sim 27.3$ in S1 and $F814W \sim 28.0$ in S2. To avoid large incompleteness corrections, we focus most of our analysis on the common CMD region where both fields have $\gtrsim 60\%$ completeness. We note that the faintest sources measured in S2 are about 0.5 mag brighter than in S1 despite identical exposure times. This difference is due to a much smaller angle between the Sun and the telescope’s optical axis during the S2 observations (55° for S2 vs. 110° for S1), resulting in a sky background about 2 times brighter in S2 than in S1. Finally, we expect the number of foreground stars to be small in both fields. The Besancon model of the Milky Way (Robin et al. 2003) predicts only ~ 15 foreground stars in the region defined by $0 < (F606W - F814W) < 1$ and $25 < F814W < 29$.

3 COLOUR-MAGNITUDE DIAGRAMS

We begin with a qualitative inspection of the CMDs, to be followed by a more detailed derivation of the SFH in §4. Fig. 3 shows the BaSTI theoretical isochrones (Pietrinferni et al. 2004) overplotted on the CMDs adopting a distance modulus of $(m - M)_0 = 24.69$ (Galleti et al. 2004). For the reddening, we adopt the Schlegel et al. (1998) maps and the ACS filter extinction ratios for a G2V star (Sirianni et al. 2005). The average values for S1 and S2 are $E(F606W - F814W) = 0.04$ and $A_{F814} = 0.08$, which are within 0.01 mag of the values for each field individually. The isochrones have a metallicity of $[M/H] = -0.7$ dex and ages of 0.2, 0.32, 0.5, 1.0, 2.0, 3.2, 6.3, and 12.6 Gyr. We use $[M/H] = -0.7$ dex as a fiducial

¹ DOLPHOT is an adaptation of the photometry package HSTphot (Dolphin 2000). It can be downloaded from <http://purcell.as.arizona.edu/dolphot/>.

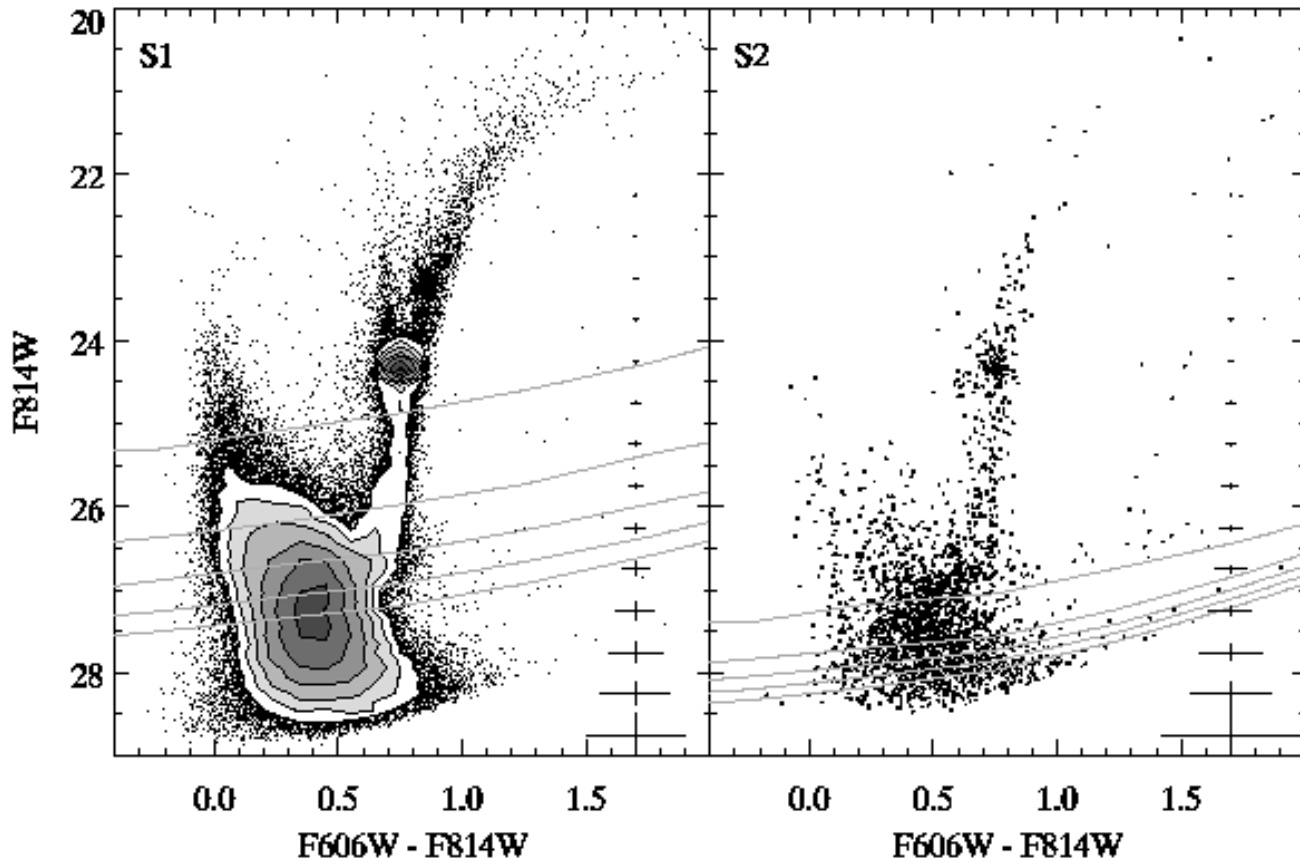


Figure 2. CMD of field S1 (left) at 9.1 kpc and S2 (right) at 11.6 kpc. The contour levels are $[1.0, 1.5, 2.25, 3.4, 5.1, 7.65, 11.5] \times 10^4 \text{mag}^{-2}$. The error bars on the right side of each panel show median errors derived from artificial star tests. The solid gray lines from top to bottom denote the 90, 80, 70, 60, and 50% completeness levels.

value for both fields in Fig. 3 because it roughly matches most of the CMD features and provides a useful starting point for a comparative discussion. Throughout this paper we use the common approximation for metallicity, $[M/H] \approx \log(Z/Z_{\odot})$ where $Z_{\odot} = 0.019$.

The sub-giant branch (SGB) is one of the most age-sensitive and well-understood stellar evolutionary phases. Field S1 has a prominent SGB which separates from the main sequence (MS) at $F814W \sim 26.75$ while the SGB in S2 is ~ 0.25 mag fainter. Visual inspection of the shape and position of the SGB suggests a significant fraction of stars < 6 Gyr old in both fields, consistent with several other properties of the CMDs. For example, the mean de-reddened colour and magnitude of the S1 red clump (RC) in the Johnson-Cousins system are $(V - I)_0 = 0.92 \pm 0.01$ and $M_I = -0.44 \pm 0.02$. These values differ in S2 by no more than 0.03 mag. According to the empirical calibration of red horizontal branch stars made by Chen et al. (2009), the RC colour and magnitude give an age of $\sim 4 - 6$ Gyr assuming $[\text{Fe}/\text{H}] \sim -0.6$ dex, although it should be noted that their calibrating open cluster sample contained no clusters with ages less than 8 Gyr and only one with $[\text{Fe}/\text{H}] > -0.7$ dex. According to the models of Girardi & Salaris (2001), the RC magnitude is consistent with ages $\lesssim 5$ Gyr for $[M/H] > -1.7$ dex and an age of ~ 3 Gyr for $[M/H] = -0.7$ dex. Similarly, the colour is consistent with ages $\sim 1 - 6$ Gyr

and $[M/H] \sim -0.8$ to -0.4 dex. The stellar models predict the RC magnitude to fade with increasing age and metallicity for ages $\lesssim 10$ Gyr. The colour distribution of RGB stars in S2 is marginally bluer than in S1, with a K-S test giving a probability of 6% that they are drawn from the same parent distribution. Hence, if S2 is older than S1, as indicated by the SGB, then it would also have to be more metal-poor to have nearly the same RC magnitude and RGB colour.

The number of asymptotic giant branch (AGB) stars above the red giant branch (RGB) tip is another age indicator because their lifetime increases with decreasing mass (Martínez-Delgado et al. 1999). Elston & Silva (1992) estimated the ratio of the number of AGB stars within one magnitude above the RGB tip to the number of first ascent RGB stars within one magnitude below the tip to be $0.17 - 0.25$ in the presence of a significant population with an age of 2 - 4 Gyr. Although there are too few stars to calculate this ratio in S2, we find a value of 0.31 ± 0.15 (random) in S1, again suggestive of a large intermediate-age population.

There is no obvious horizontal branch (HB) of an old, metal-poor population in the CMDs of S1 or S2. However, this feature could be lost amongst the MS stars and bright SGB stars crossing the Hertzsprung Gap. The presence of RR Lyrae (RRL) variable stars would unequivocally signal an ancient ($\gtrsim 10$ Gyr) population. Our observations were not optimized for determining precise RRL properties, but

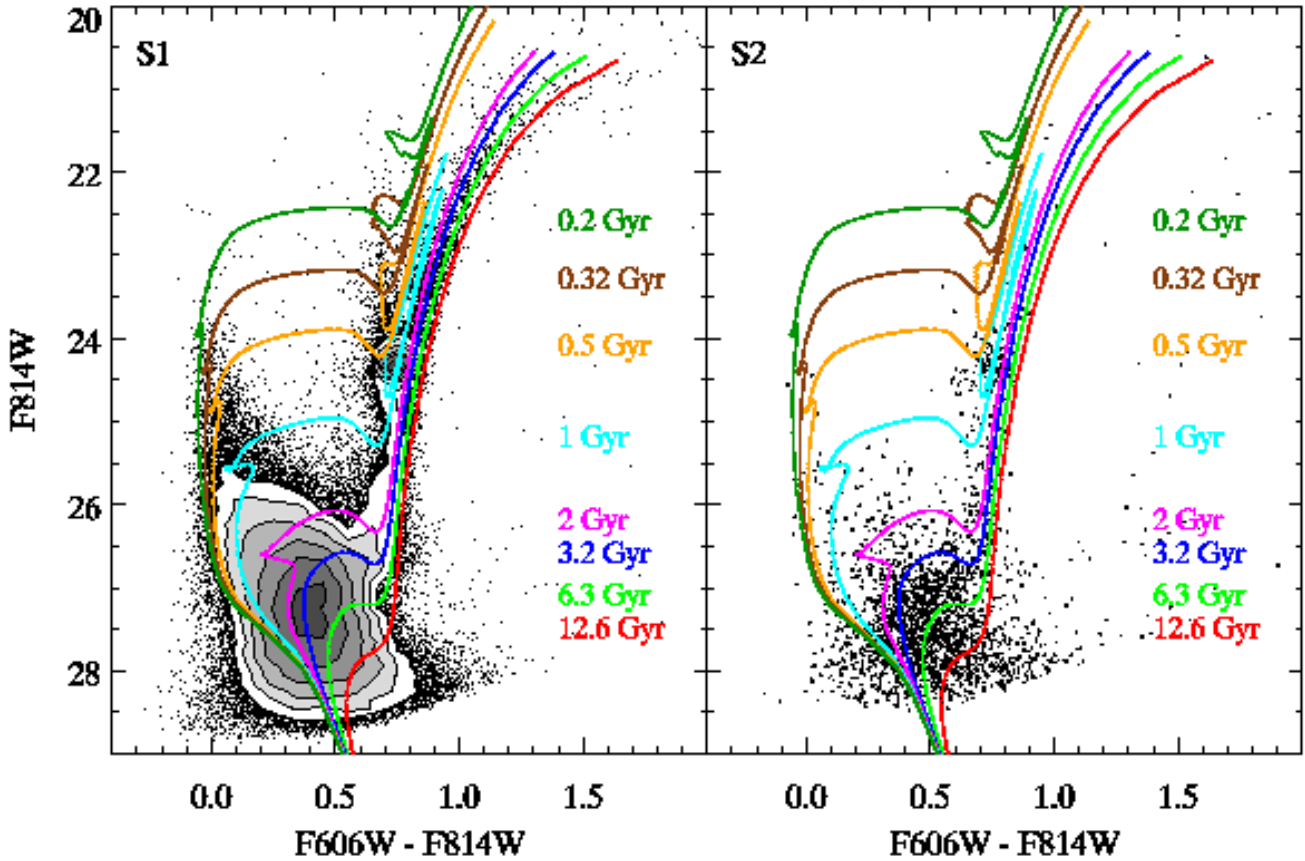


Figure 3. CMDs with BaSTI theoretical isochrones overplotted. The isochrones have $[M/H] = -0.7$ dex and age = 0.2, 0.32, 0.5, 1, 2, 3.2, 6.3, and 12.6 Gyr from top to bottom. The contours are the same as in Fig. 2. The magnitude of the SGB in both CMDs indicates a significant population $\lesssim 6$ Gyr old.

we still have enough epochs (24 spaced over ~ 5 [7] days in S1 [S2]) to search for and identify candidates based on their photometric variability.

To that end, we used the Stetson (1996) variability index, L , which measures correlated magnitude residuals in pairs of observations and is robust to outlier data points. In S1, there were 5 stars with L values $\gtrsim 3\sigma$ above the mean at $F606W \sim 25 - 26$ and lying near the instability strip at $(F606W - F814W) \sim 0.25 - 0.5$ (Brown et al. 2004; Bernard et al. 2009). In S2, there were no such stars. Fig. 4 shows the phased light curves and coordinates of the S1 RRL candidates after fitting the templates of Layden (1998) and Layden & Sarajedini (2000). The fact that we find more candidates in S1 than in S2 suggests S1 had a higher star formation rate (SFR) or a lower metallicity at ages $\gtrsim 10$ Gyr, but given the small samples involved and sparse phase coverage, it is difficult to make any firm conclusion on this matter.

3.1 Colour Function

Gallagher (1996) and Gallart et al. (2005) have shown how the colour function (CF) is a powerful probe of the SFH because the main sequence turn-off (MSTO) and SGB temperature decreases with age. The left panel of Fig. 5 compares the CF summed over the magnitude range $21 < F814W <$

27 in S1 (solid black line) and S2 (dashed black line). The magenta line shows a model generated with IAC-star (see §4.1 for further details) for a constant metallicity $[M/H] = -0.5$ dex with no metallicity spread and constant SFR from 0 – 14 Gyr after convolution with the photometric errors and completeness. The other lines show the contributions of several different age ranges to the total model.

Concentrating on the left panel in Fig. 5, the CF for most age-groups displays two peaks: a blue peak at $(F606W - F814W) \sim 0 - 0.4$ that is associated with the MSTO and SGB of young and intermediate ages and a red peak at $(F606W - F814W) \sim 0.75$ that is dominated by the RC and RGB. The data and total model CFs are normalised to the heights of their red peaks. The relative heights of the red and blue peaks and the position of the blue peak vary with age and metallicity. Ages < 1 Gyr contribute mostly to the blue peak while ages > 8 Gyr contribute entirely to the red peak. At intermediate ages, the blue peak shifts to redder colours and the blue/red peak height ratio decreases.

The blue envelope in the total model is too blue and the red peak is too red by ~ 0.05 mag, perhaps indicating (1) that the metallicity should be higher and lower for, respectively, the youngest and oldest ages, (2) that the bolometric corrections have a small zero-point offset at low or high temperatures, or (3) that the reddening should be higher for blue stars and lower for red stars. The value $[M/H] = -0.5$ dex

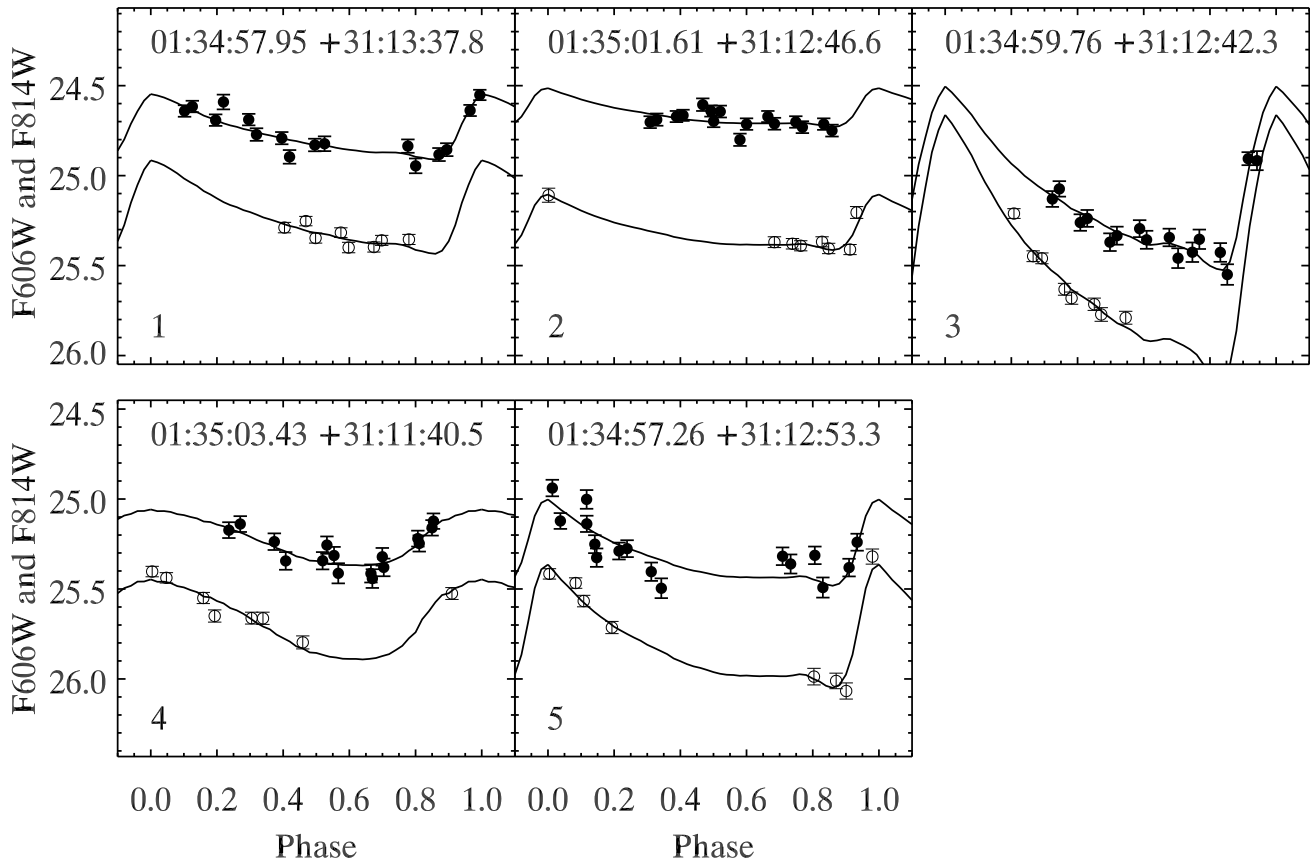


Figure 4. Example template fits to the light curves of the 5 RRL candidates in S1. Open points are the $F606W$ -band and solid points are the $F814W$ -band. The J2000.0 coordinates are given at the top of each panel.

provides a reasonable match to the entire CF and is useful for illustrating the dominance of intermediate ages. These considerations do not significantly change if the metallicity varies by ~ 0.3 dex, which would mainly act to shift the CF left or right rather than change the relative peak heights. Because a constant metallicity with zero spread may not apply to the system’s entire chemical enrichment history, we also tried a piecewise linear age-metallicity relation increasing from -1.2 dex at 14 Gyr, to -0.7 dex at 8 Gyr, and to -0.5 dex at the present-day with a uniform metallicity spread of ± 0.1 dex. The resulting model CF was slightly more similar to the original in that the position of the red peak more closely matched the data.

As the left panel of Fig. 5 shows, a constant SFR provides a relatively poor fit to the CF of both S1 and S2. Any arbitrary SFH can be approximated by scaling the age-group curves accordingly and then renormalising the sum to the red peak’s new height. For example, an exponentially increasing SFR from 14 Gyr ago to the present would preferentially raise younger age-group curves by larger amounts and make the blue envelope of the CF too high. In S1, the position of the blue peak and its height relative to the red peak are most closely matched by the 1 – 4 Gyr age range. This is more clearly seen in the right panel of Fig. 5, which shows the CFs for ages 1 – 4 Gyr and 1 – 8 Gyr after normalising them to their red peaks. Crucially, this means that ages 1 – 4 Gyr can account for the majority of the SGB,

RC, and RGB stars in S1 and that there is little room for stars older than 8 Gyr, which would push up the red peak without changing the height of the blue peak. The lack of a strong blue peak in S2 again suggests an older population than in S1.

3.2 Vertical Clump Morphology

Finally, we examine how a particular feature of the S1 CMD can constrain the metallicity of young stars in S1. At ages of $\sim 0.4 - 1.2$ Gyr, stars with masses in the range $\sim 2 - 3 M_{\odot}$ form a vertical clump that extends from and partially overlaps with the left-hand side of the RC. The slope of this vertical clump depends on metallicity while its extension below the RC appears only for $[M/H] \gtrsim -0.7$ dex (Gallart et al. 2005). Fig. 6 shows how the morphology of the vertical clump constrains the metallicity at these ages. In the left-hand column are three synthetic CMDs generated with IACstar (see §4.1 for further details) assuming a constant SFR from 0 – 14 Gyr. From top to bottom, the panels in the left-hand column assume a constant metallicity of $[M/H] = -1.0$, -0.5 , and 0.0 dex with no metallicity spread. The right-hand column shows the S1 CMD. The solid lines in each panel are meant to guide the reader’s eye. The synthetic stars are colour-coded by three age ranges, 0 – 1.2 Gyr (blue), 1.2 – 8 Gyr (black), and > 8 Gyr (red). This figure demonstrates that the slope, length, and position of the vertical clump are

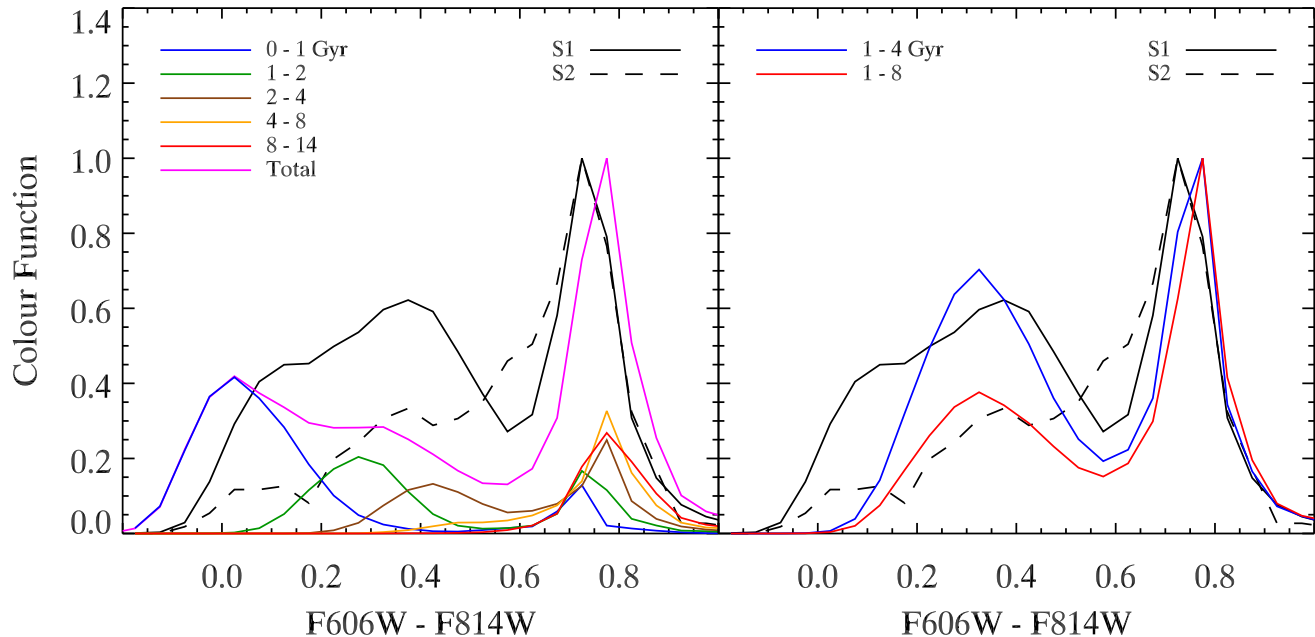


Figure 5. CF in S1 (solid black line) and S2 (dashed black line) summed over the magnitude range $21 < F814W < 27$. The coloured lines show model CFs for different age ranges assuming a constant SFR and $[M/H] = -0.5$ dex and no metallicity spread. (Left) The total model CF of all ages is represented by the magenta line. The data and total model CFs are normalised to their red peaks. (Right) The model CFs for ages 1 – 4 Gyr and 1 – 8 Gyr are normalised to their red peaks. The position of the blue peak and its height relative to the red peak indicate a dominant population with ages $\sim 1 - 4$ Gyr in S1 and an older population in S2.

best matched by $[M/H] \sim -0.5$ dex, as is the position of the blue plume in the lower-left corner of each panel. The match is not perfect, but this is not surprising since the stellar tracks or bolometric corrections may have zero-point offsets in colour and magnitude and, for this test, the metallicity was constant with no spread. It is also worth noting that the slope of the RGB and morphology of the RC are best matched by the same metallicity, especially if we exclude stars older than 8 Gyr.

In summary, various features of the S1 CMD point to a dominant population with ages $\sim 1 - 4$ Gyr, and, at younger ages, a metallicity > -0.7 . The fainter SGB, but similar RC magnitude and RGB colour in S2 indicate an older and more metal-poor population.

4 STAR FORMATION HISTORY

4.1 Method

To obtain a more detailed look at the mix of ages and metallicities in these fields, we used the method of synthetic CMD fitting. This method involved fitting the observed CMD with a linear combination of individual basis populations each representing a range of ages and metallicities. The coefficients of the linear combination gave the SFRs at their respective ages and metallicities. Various implementations of this technique have been used extensively over the years (e.g., Tosi et al. 1991; Bertelli et al. 1992; Tolstoy & Saha 1996; Aparicio et al. 1997; Gallart et al. 1999; Hernandez et al. 2000; Harris & Zaritsky 2001; Holtzman et al. 1999;

Dolphin 2002; Cole et al. 2007; Aparicio & Hidalgo 2009) and in this paper we followed closely that of B07.

The basis population CMDs were generated with IAC-star (Aparicio & Gallart 2004) and then convolved with the photometric errors and completeness rates derived from the artificial star tests. The entire set of basis CMDs spanned ages from 25.1 Myr to 14.1 Gyr and metallicities from -1.7 to $+0.1$ dex. The age range was broken up into 13 bins whose widths increased with age because the photometric spacing between stellar isochrones decreases as they get older. The metallicity range was divided into 6 uniform bins each 0.3 dex wide. We adopted the BaSTI theoretical stellar evolutionary tracks (Pietrinferni et al. 2004, called Teramo in IAC-star) with mass loss parameter $\eta = 0.4$ and ACS bolometric corrections. We note that using the Girardi et al. (2000) tracks gave similar results with a tendency for a mean overall metallicity ~ 0.2 dex lower than the BaSTI tracks. We take this as an indication of the systematic error on our metallicities.

For the IMF, we adopted a Salpeter law from 0.1 to $120 M_{\odot}$. Other IMFs that turn over at low masses would mainly act to change the overall normalization of the SFH rather than its shape. The other input parameters were the binary fraction and minimum binary mass ratio, both of which we set to 0.5. Gallart et al. (1999) summarized observational evidence supporting similar values. Tests whereby we fit mock populations with known parameters did not reveal any systematic effects that might arise from an incorrect binary fraction. The fitting region in the CMDs spanned the colour range $-0.5 < (F606W - F814W) < 2.0$ and the magnitude range $21 < F814W < 27$ where both fields are $\gtrsim 60\%$ complete. Including fainter magnitudes resulted in poorer fits,

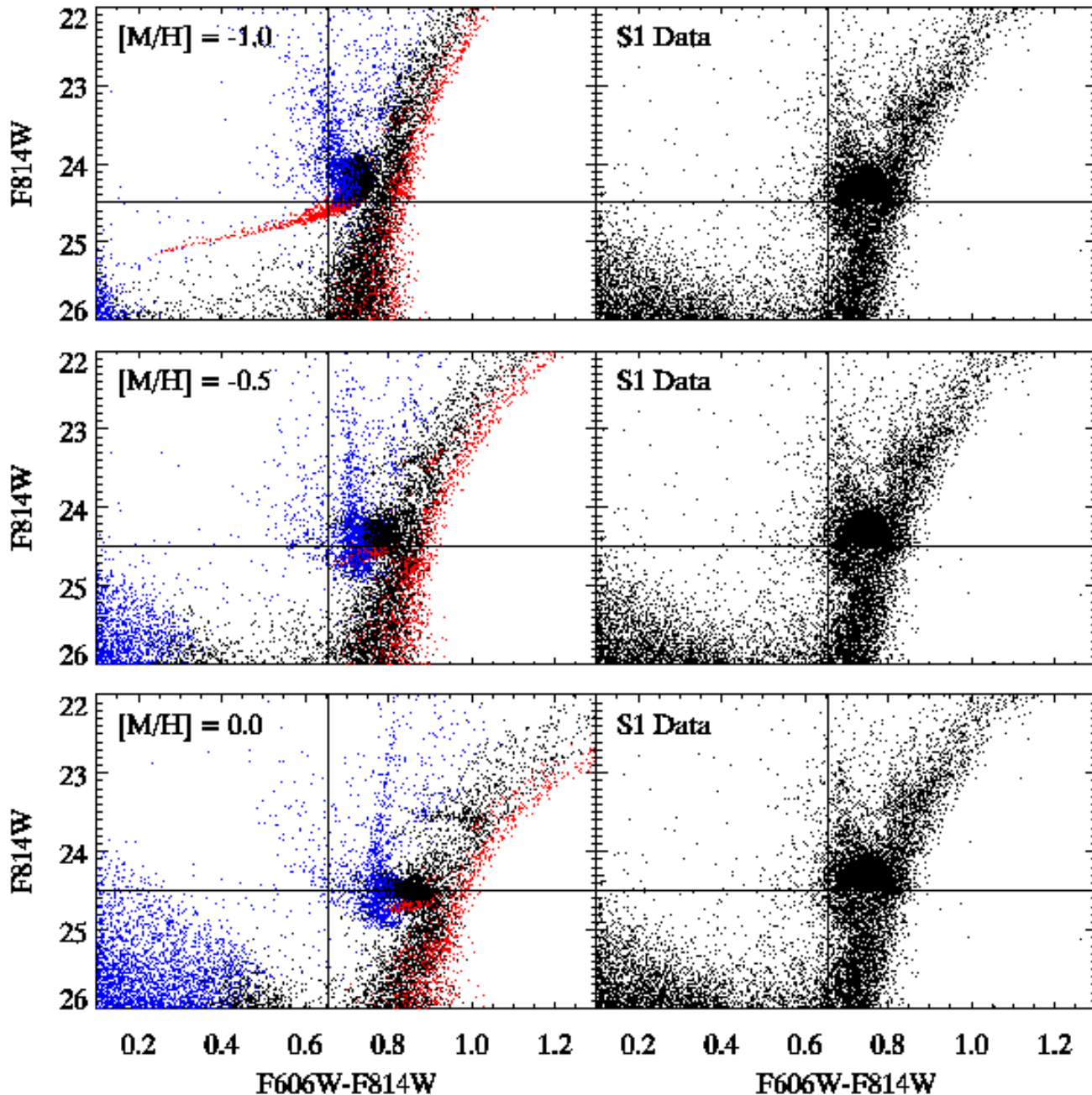


Figure 6. Using the morphology of the vertical clump to constrain metallicity. The right-hand column shows the data for S1 and the left-hand column shows, from top to bottom, synthetic CMDs for $[M/H] = -1.0$, -0.5 , and 0.0 dex and constant SFR. The points in the synthetic CMDs are divided into the age ranges 8 – 14 Gyr (red), 1.2 – 8 Gyr (black), and < 1.2 Gyr (blue). The solid lines are meant to guide the reader’s eye. The morphology of the vertical clump and its extension below the RC are best matched by $[M/H] \sim -0.5$ dex.

but broadly similar SFHs. Within the fitting region, the data and model CMDs were divided into square boxes 0.1 mag on a side.

We tried masking the RC and upper RGB ($F814W < 25$) from the fits and the solutions were again similar to the originals using both the BaSTI and Girardi tracks. We also found that the differences between the BaSTI and Girardi solutions were smaller when including the RC and upper RGB in the fits. We think that this is because, by using more of the CMD regions available, we effectively average

over their systematic errors and are not as vulnerable to the errors in any one particular region. It is possible, however, that a different approach would be necessary for deeper data or other stellar systems populating different regions of the age-metallicity plane. In all the tests we conducted, the fraction of stars formed over 4.5 Gyr ago in both fields differed from the original BaSTI solution by $\lesssim 10\%$ and the mean age differed by a few tenths of a Gyr. To be conservative, we take 1 Gyr as the systematic uncertainty on the mean age.

We used the StarFISH software package (Harris &

Zaritsky 2001) to find the best-fitting model according to a maximum likelihood statistic appropriate for Poisson-distributed data (Dolphin 2002). StarFISH uses a downhill simplex algorithm to search through parameter space and locate the best fit. The stock implementation of this algorithm employs a random search through parameter space to locate a reasonable starting position for the simplex. Instead of using this random search, we initialized the simplex to the best-fitting solution found by the genetic algorithm PIKAIA (Charbonneau 1995). For consistency, we applied this hybrid approach to both fields although it made no difference to the solutions for S1. When applied to S2, the hybrid approach was less prone to getting stuck in local minima, but the solutions were consistent with those of the stock implementation to within the errors.

StarFISH computed the error bars in a 3-stage process designed to measure the independent as well as correlated errors between coefficients (Harris & Zaritsky 2001, 2004). First, individual coefficients were varied while holding all others fixed at their best-fit values. Second, adjacent pairs of coefficients were varied holding the rest fixed at their best-fit values, and, third, all coefficients were varied simultaneously. At each stage, the program iteratively stepped away from the best-fit and computed the new likelihood ratio until this ratio reached its 1σ limit. Throughout the whole process, the program updated and stored the maximum variation of every coefficient resulting in the 1σ limit. The final maximum variations were taken as the 1σ confidence intervals for the coefficients.

As a zero-order correction to any possible errors in the stellar tracks or bolometric corrections, we also solved for distance and extinction. The distance modulus was varied from 24.40 – 24.90 in steps of 0.1 and the $F606W$ extinction was varied from 0.00 – 0.30 in steps of 0.05. All acceptable solutions on this grid were averaged together and their dispersion was added in quadrature with the error bars of the best individual solution. With this procedure, the final error bars include random and correlated errors of the SFH amplitudes as well as zero-point uncertainty in the stellar tracks and bolometric corrections. The error bars do not necessarily reflect the variation of the true SFR within an age bin, but rather the 1σ confidence interval on the SFR averaged over an age bin.

4.2 Results

Figures 7–8 present the results of the CMD fitting analysis. The recovered SFHs are in line with our qualitative expectations from §3. In field S1, the mean age is 3.2 Gyr and most of the star formation took place $\sim 2-4$ Gyr ago, coinciding with a general peak in the SFR. The decline in the SFR over the past 1 Gyr is a robust result because a constant SFR would produce too many stars on the blue plume at ($F606W - F814W$) ~ 0.0 as found from the CF analysis. The age of the SFR peak is similar to that measured by B07, but we must be careful not to over-interpret this feature in the solutions. Any CMD fitting analysis is limited in its ability to measure the burstiness of the underlying SFH. Short bursts with timescales smaller than the age bins will be heavily smoothed. Longer bursts occurring over several age bins will be more reliably recovered, but the recovered peaks may drift by one age bin due to the finite model bin-

ning and errors in the model input parameters. We found that using smaller age and metallicity bins or shifting the bins by a fractional amount did not change the general picture of a period of enhanced SFR $\sim 2-4$ Gyr ago and had only a small effect on the mean age, at the level of ~ 0.5 Gyr.

In field S1, the mean SFR over all ages is $2.6 \times 10^{-4} M_{\odot} \text{ yr}^{-1}$ and the mean SFR at ages < 8 Gyr is $4.5 \times 10^{-4} M_{\odot} \text{ yr}^{-1}$. The total stellar mass formed is $3.6 \times 10^6 M_{\odot}$ resulting in a projected stellar surface density of $\sim 5 M_{\odot} \text{ pc}^{-2}$. Correcting for an inclination of 56° yields a stellar surface density of $\sim 2.7 M_{\odot} \text{ pc}^{-2}$ in the disc plane. Repeating the fit with an IMF that turns over at $0.5 M_{\odot}$ (Kroupa 2002) gave a stellar surface density $\sim 25\%$ lower, but the relative age distribution was unchanged. The best-fitting distance modulus is 24.72 ± 0.09 , in good agreement with the Galleti et al. (2004) value. The best-fitting extinction is $A_{F606W} = 0.05 \pm 0.03$, lower than the Schlegel et al. (1998) value of 0.12. This difference probably reflects a zero-point offset in the stellar evolutionary tracks or bolometric corrections as was hinted at in the analysis of the vertical clump feature in §3 and in Fig. 6 or it could reflect small scale reddening variations not captured by the Schlegel et al. (1998) maps.

The cumulative age distribution in panel (b) is actually more stable against correlations between age bins than the differential SFH in panel (a). Roughly 85% of stars in S1 formed by 1.5 Gyr ago and $\sim 65\%$ formed by 2.5 Gyr ago. Only 14% of stars have ages > 4.5 Gyr, but this value could be as low as 0% or as high as 28% and still provide a fit consistent with the original at the 1σ level.

There is a trend of decreasing metallicity with age between 0.35 and 6.2 Gyr in S1 as expected in normal chemical evolution scenarios. However, the trend is weak and consistent with no evolution over most of the history, and it partially relies on the RC/RGB morphology. After repeating the fit with the RC and upper RGB masked, the new S1 age-metallicity relation did not continuously decrease from 2.0 to 6.2 Gyr, but it was consistent with the original at the 1σ level or differed by < 0.2 dex in all age bins. Because of the weak metallicity evolution, the metallicity distribution is narrow, with $\sim 90\%$ of stars having $[M/H]$ between -0.8 and -0.2 dex. The mean metallicity of all stars ever formed is $[M/H] = -0.47_{-0.05}^{+0.03}$ dex. These error bars represent only the formal random error, but the systematic error is ~ 0.2 dex. The lack of stars with $[M/H] < -0.8$ dex may be the result of pre-enrichment of the gas out of which most stars formed. The metallicity at 0.6 – 1.1 Gyr is ~ -0.4 dex, in reasonable agreement with our analysis of the vertical clump morphology in §3.2. Because there is such a small signal in the oldest 2 bins, their metallicities are completely unconstrained. Likewise, there are not enough stars at ages < 0.35 Gyr to populate the metallicity-sensitive core helium burning (blue loop) phase, and, consequently, the age-metallicity relation is also unconstrained at these ages.

The metallicity in S1 drops from -0.13 ± 0.11 dex at 0.35 Gyr to -0.36 ± 0.10 dex at 0.62 Gyr. The latter value may be a better indicator of the present-day metallicity because it is constrained by the metallicity-sensitive position and morphology of the vertical clump whereas the former value comes primarily from the colour of the upper MS, which varies little with metallicity. Extrapolation of the

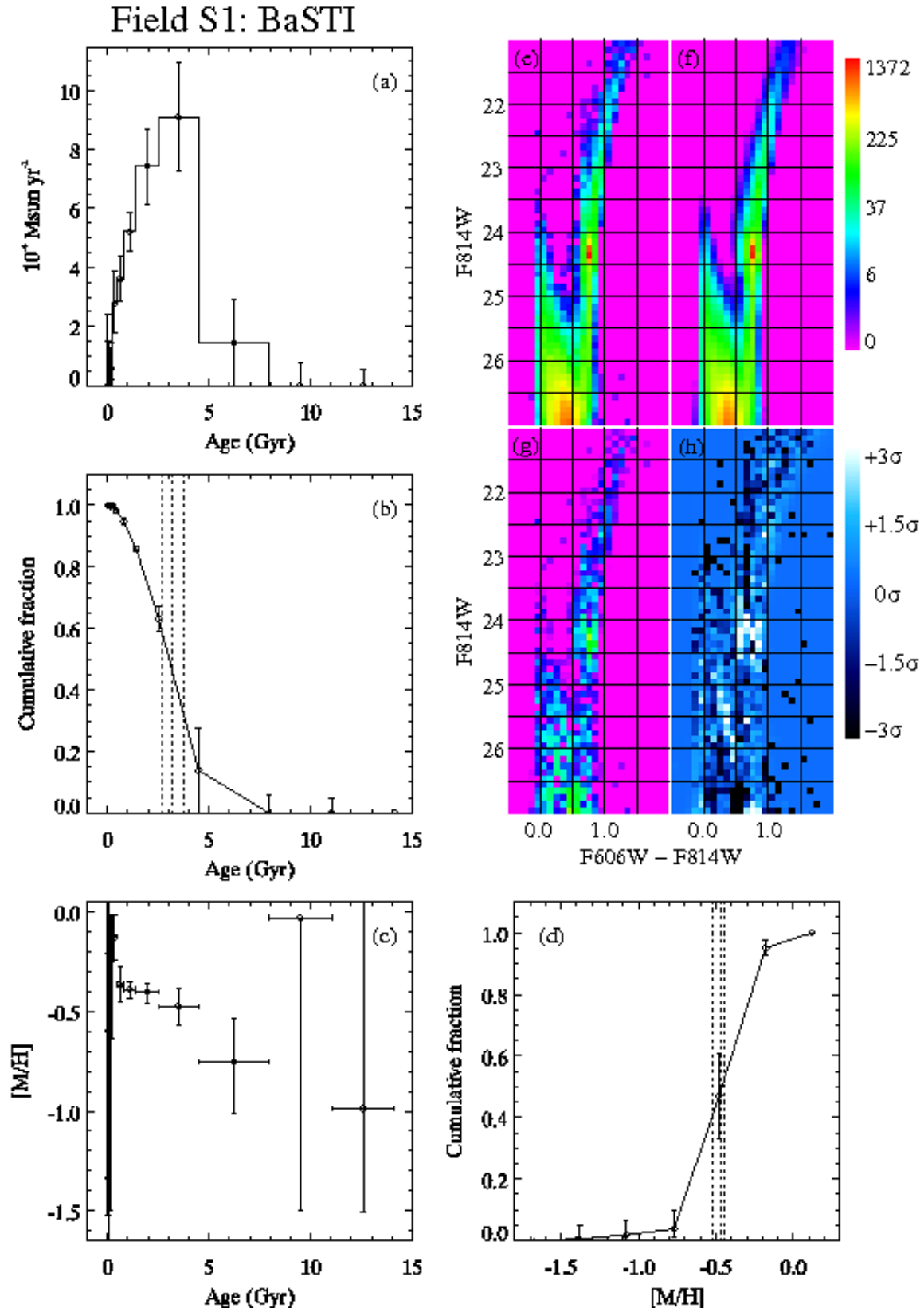


Figure 7. The SFH of field S1. The panels show (a) the SFH, (b) the cumulative age distribution, (c) the age-metallicity relation, (d) the cumulative metallicity distribution, (e) the data CMD, (f) the model CMD, (g) the absolute magnitude of the residuals, and (h) the significance of the residuals. Panels (e) – (g) use the same logarithmic intensity scale. The intensity scale in (h) goes from -3σ (black) to $+3\sigma$ (white) where negative values indicate the model is too low. The vertical dotted lines in (b) and (d) are mean values and their 1σ confidence intervals.

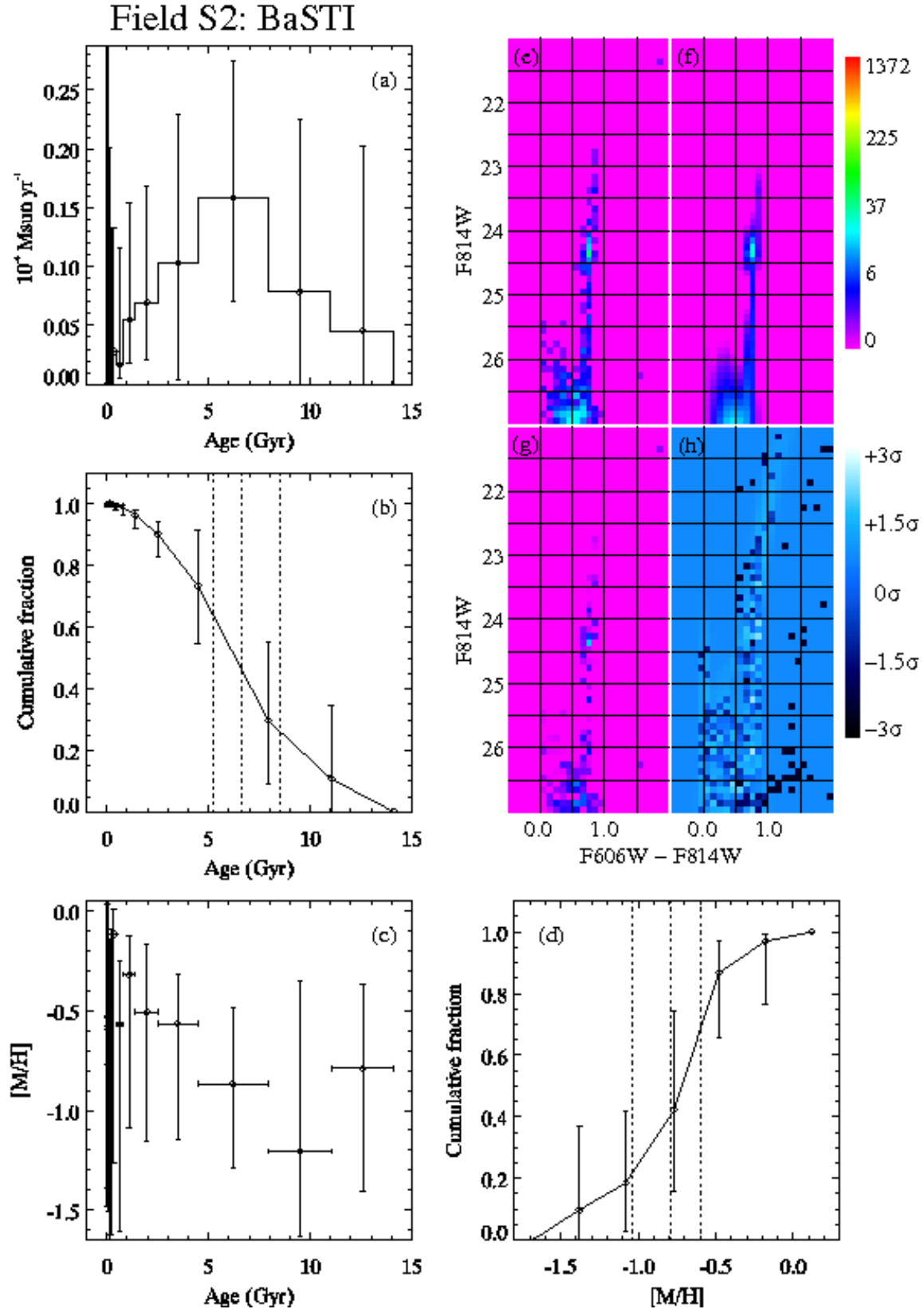


Figure 8. The SFH of field S2. The panels show the same information as Fig. 7. Note that the y-axis range in panel (a) is reduced compared to Fig. 7. The 1σ upper limits on the SFRs in the first, second, and third youngest age bins in panel (a) extend off the top of the graph. Their values are 0.9, 0.5, and $0.3 \times 10^{-4} M_{\odot} \text{ yr}^{-1}$, respectively.

metallicity gradient in M33 measured by U et al. (2009) from A- and B-type supergiants at $R_{dp} \lesssim 7$ kpc predicts a lower present-day value in S1, $[M/H] = -0.65 \pm 0.13$ dex. The HII region and planetary nebula gradients computed by Bresolin et al. (2010) predict $[O/H] = -0.54 \pm 0.10$ dex and $[O/H] = -0.34 \pm 0.20$ dex, respectively, when extrapolating beyond their outermost measurements at $R_{dp} \sim 8$ kpc and adopting the solar oxygen abundance of Asplund et al. (2009). Using the solar oxygen abundance of Grevesse & Sauval (1998) would shift their measurements down by ~ 0.1 dex. The discrepancy between our measurement and theirs could mean that the metallicity gradient flattens out beyond the outermost measured supergiants, HII regions, and planetary nebulae, or that M33's inner disc has accreted metal-poor gas in the last 0.35 Gyr.

Compared to field S1, S2 is older and more metal-poor, but the small number of stars in this field limit the statistical significance of this result. The interquartile age range in S2 is $\sim 4 - 9$ Gyr, $\sim 75\%$ of stars have ages > 4.5 Gyr, and $\sim 90\%$ have ages > 2.5 Gyr. Most stars have metallicities between -1.0 and -0.5 dex. The mean SFR over all ages is $8.9 \times 10^{-6} M_{\odot} \text{ yr}^{-1}$. The total stellar mass formed is ~ 30 times less than in S1, or $1.2 \times 10^5 M_{\odot}$, resulting in projected and deprojected stellar surface densities of $\sim 0.18 M_{\odot} \text{ pc}^{-2}$ and $\sim 0.10 M_{\odot} \text{ pc}^{-2}$, respectively, assuming the same inclination as in S1. The best-fitting distance modulus is 24.69 ± 0.09 and the best-fitting extinction is $A_{F606W} = 0.04 \pm 0.05$, in good agreement with those found for field S1.

In §3, we identified 5 RRL candidates in S1 and none in S2. Are the derived SFHs for S1 and S2 consistent with this finding? In field S1, the 1σ upper limit on the SFR in the oldest age bin at 12.6 Gyr yields $\sim 1.7 \times 10^5 M_{\odot}$ of integrated star formation. In S2, this value is $\sim 5.0 \times 10^4 M_{\odot}$. From the synthetic CMDs in our library, we estimate that a 10,000 M_{\odot} population with age $\gtrsim 8$ Gyr and $[M/H] \lesssim -0.4$ contains ~ 4 HB stars regardless of HB morphology and with little dependence on metallicity. This yields a 1σ upper limit of ~ 70 HB stars in S1 and ~ 20 HB stars in S2. Given that we expect the RRL to be a subset of the total number of HB stars, the number of RRL candidates we found in S1 and S2 is well within the 1σ uncertainty in the SFR of the oldest age bin.

5 DISCUSSION

The CMD fitting analysis indicates that almost the entire stellar mass in S1 formed in the last 8 Gyr and that field S2 is older and more metal-poor. Fig. 9 compares the cumulative age distributions of both fields. The shaded regions represent the 1σ confidence intervals assuming a constant SFR within each age bin. From this comparison, it is likely that S2 has always been older than S1, but given the depth of our photometry, we cannot say precisely when star formation started in each field. The 1σ errors allow for nearly the same fraction of stars > 8 Gyr old in both S1 and S2, so it is feasible that star formation in S1 started at the same time as or even before it did in S2. However, the fraction of ancient stars is unlikely to be significantly larger in S1 than in S2.

Fig. 9 also shows the results of W09b for their 4 fields

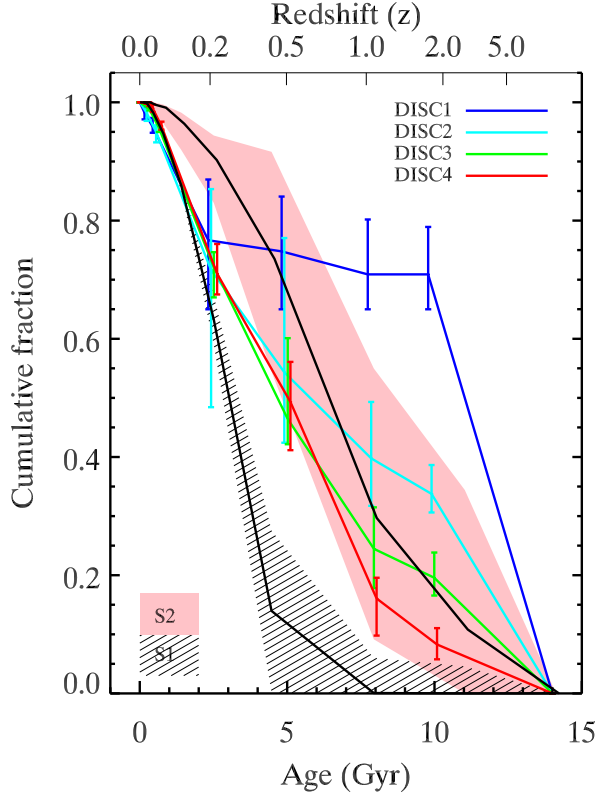


Figure 9. Cumulative age distributions for fields S1 and S2 (black lines). Their 1σ confidence intervals are displayed as shaded regions assuming a constant SFR within each age bin. From top to bottom, the four solid lines with error bars are the results of W09b covering $R_{dp} \sim 1 - 6$ kpc. Field S1 is younger than their outermost field (DISC4). Field S2 is older than S1 and this difference is not just in the recent SFH, but likely stretches back over their entire histories.

at $R_{dp} \sim 1 - 6$ kpc. The cumulative star formation in S1 is less than in the W09b outermost field (DISC4) at nearly all ages, demonstrating that the inside-out growth of M33's inner disc extends all the way to the disc edge. In addition, the difference in SFH between S1 and S2 adds further support to the idea that M33's age gradient reverses at large radii near the break radius.

5.1 Explanations for M33's Age Gradient

There are several possible explanations for the behavior of M33's mean age profile. The one favoured by W09b involved the secular redistribution of stars seen in recent simulations of isolated disc formation and evolution (Roškar et al. 2008b). In these simulations, inside-out disc growth leads to a negative age gradient within the break radius, but radial mixing of stars due to interactions with transient spiral density waves causes a positive age gradient beyond the break radius.

If this scenario is true, then most of the stars in S2 formed at smaller radii and the ages of the youngest stars in S2 could constrain the stellar migration timescale. Inspection of the S2 CMD and SFH shows that the youngest stars are likely to have ages < 1 Gyr. There are a few stars that lie near the 200 Myr isochrone in the right panel of

Fig. 3, but according to the Besancon model for the MW (Robin et al. 2003), the brightest of these (at $F814W \sim 22$) may be foreground stars. A migration timescale of $\sim 0.2 - 1$ Gyr appears consistent with the simulation of Roškar et al. (2008b), in which the disc break appears quickly. However, the youngest stars, which represent a small fraction of the total in S2, may have formed in-situ. If so, then they formed at sub-threshold gas densities. Typical empirical and theoretical estimates of the star formation threshold lie in the range $\sim 3 - 10 M_{\odot} \text{ pc}^{-2}$ (Skillman 1987; Taylor et al. 1994; Ferguson et al. 1998; Martin & Kennicutt 2001; Elmegreen & Parravano 1994; Schaye 2004), but the HI density in S2 is only $0.1 M_{\odot} \text{ pc}^{-2}$ (Thilker et al. 2002, D. Thilker, private communication). In comparison, field S1 is more gas-rich with an HI density of $4.1 M_{\odot} \text{ pc}^{-2}$ (Thilker et al. 2002, D. Thilker, private communication), so the youngest stars in S1 could have formed in-situ without violating previous estimates of the SF threshold.

The radial mixing in the above scenario can cause the measured SFH in any one region of a galaxy to differ from the true one, especially in the outermost disc regions. Roškar et al. (2008a) found a nearly constant measured SFH near the break radius of their simulated galaxy whereas the true SFH was significantly skewed toward younger ages. Our measured SFH in S1 strongly rules out a constant SFH and is actually more consistent with their true SFH. In addition, field S1 is unlikely to be significantly contaminated by stars that migrated from the inner disc because of the small fraction of stars older than 4.5 Gyr ($\sim 14\%$) relative to the inner disc where such stars are common ($\gtrsim 50\%$; W09b).

Aside from stellar radial mixing, there are other possible explanations for the behaviour of M33's mean age profile. Sánchez-Blázquez et al. (2009) studied the formation of an early type spiral galaxy in a high resolution cosmological simulation. This galaxy exhibited a break in the exponential radial SB profile analogous to that in M33, but the stellar mass density profile exhibited no such break because of a net radial migration of stars towards the outskirts. This galaxy also had an upturn in the age gradient at the break radius, but Sánchez-Blázquez et al. (2009) argued that this was caused not by the radial migration, but by a warp in the gas disc and a concurrent drop in gas volume density and SFR. It is well known that the gas disc of M33 begins to warp near the edge of the optical disc (Rogstad et al. 1976; Corbelli & Schneider 1997), lending support to this alternative scenario. However, contrary to the simulations of Sánchez-Blázquez et al. (2009) and Martínez-Serrano et al. (2009), we find that M33 has a sharp drop in the stellar mass density near the break radius.

A change in the SF efficiency may also explain the upturn in M33's age profile. Such a change might be expected to occur when the gas density drops below the SF threshold, which seems to occur near M33's break radius today. A change in SF efficiency would change the relationship between gas and SFR, behaviour that has been observed in the outskirts of spiral galaxies where the gas density is low (Bigiel et al. 2008; Leroy et al. 2008). Moreover, Leroy et al. (2008) observed a correlation of the star formation efficiency with stellar mass surface density. Thus, we would naturally expect to see a difference in SF efficiency and SFH between regions inside the break radius and regions outside it.

The older mean age beyond M33's break radius could

also be due to a transition from its thin disc to its halo or thick disc. In this case, the mean age of $\sim 6 - 8$ Gyr found in this work and in B07 for the region beyond the break would imply that the halo or thick disc is younger than it is in the MW, where these components are predominantly > 10 Gyr old (Gilmore et al. 1995; Krauss & Chaboyer 2003). The mean metallicity of -0.7 to -0.9 outside the break radius found in this study and in B07 is higher than estimates for M33's halo field stars and globular clusters, which lie in the range -1.5 to -1.3 (Sarajedini et al. 2000; McConnachie et al. 2006). It is not known whether M33 contains a thick disc, but studies of the diffuse light around galaxies have found that thick discs may be common (e.g. Burstein 1979; Morrison et al. 1997; Neeser et al. 2002; Dalcanton & Bernstein 2002). The mean age and metallicity in S2 are in the range found by Yoachim & Dalcanton (2008) for thick discs of several late-type galaxies using Lick indices.

5.2 Outer Disc Age

Finally, the results presented here suggest that the last major epoch of SF in M33's outer disc occurred $\sim 2 - 4$ Gyr ago, or at $z \sim 0.2 - 0.4$ for a standard WMAP Λ CDM cosmology (Dunkley et al. 2009). This provides a unique test of the disc assembly history predicted by cosmological N-body/SPH simulations. Most simulations until recently have focused on massive early-type spirals which may have had more active merger histories than M33, but the physical processes and timescales governing thin disc growth may be similar for a range of galaxy masses (Brooks et al. 2009).

In the simulation of Abadi et al. (2003), most stars in the thin disc formed over the last ~ 8 Gyr via the smooth, fairly constant accretion of cold gas originating in accreted satellites or dense intergalactic filaments. The thin disc mean age was ~ 7 Gyr at $R = 1$ kpc and ~ 3 Gyr at $R = 20$ kpc (or 4 disc scale-lengths). Our results for S1 are in good agreement with theirs at the same disc location in terms of disc scale-lengths, but S1 is younger than the equivalent location in their disc measured in kpc.

Sommer-Larsen et al. (2003) reported an exponentially declining rate of gas accretion onto their two simulated spiral galaxies. One galaxy formed inside-out, but had very little age gradient with a mean stellar age of $\sim 7 - 8$ Gyr. The other galaxy formed outside-in, with a mean age increasing from ~ 4 Gyr at 2 disc scale-lengths to ~ 6.5 Gyr at 6 disc scale-lengths, or $R = 10.5$ kpc. The authors did not decompose these ages into thin disc, thick disc, and halo contributions, so the ages are strictly upper limits for the thin disc, but taken at face value, they are older than what we find in S1.

Robertson et al. (2004) employed a multi-phase ISM in their cosmological simulation, resulting in the formation of a bulgeless galaxy with total mass similar to M33. However, their galaxy was older than M33 and did not simply form inside-out. The mean stellar age increased from ~ 7.5 Gyr in the nucleus to ~ 10 Gyr at 10 kpc, or 3 scale-lengths. Moreover, the stellar disc of their galaxy appeared much thicker than those of normal late-type spirals.

Governato et al. (2009) examined the formation of a bright, disc-dominated galaxy in a high resolution cosmological SPH simulation. The last major merger occurred about 6 Gyr ago, after which time an extended thin disc formed

through the accretion of cold gas from the cosmic web and cooled halo gas. This formation timescale is qualitatively consistent with what we find in M33's outer disc. Stars that formed prior to the last major merger ended up at $z = 0$ in a thick disc component with similar mass as the thin disc, but shorter scale-length.

6 CONCLUSIONS

We have analysed two HST/ACS fields at 9.1 and 11.6 kpc, straddling the break in the SB profile on M33's northern major axis. These observations offer the deepest view yet of the stellar populations in the outskirts of M33, providing a valuable observational constraint on cosmological galaxy formation simulations. Based on a CMD fitting analysis, we find that the majority of stars in both fields combined formed at $z < 1$ and that the last major epoch of star formation at the edge of M33's disc occurred at $z \sim 0.2 - 0.4$.

The mean age in the inner field, S1, is $\sim 3 \pm 1$ Gyr and the mean metallicity is $[M/H] \sim -0.5 \pm 0.2$ dex. Approximately half of all stars in S1 have ages of 2.5 – 4.5 Gyr and only $\sim 14 \pm 14\%$ have older ages. The SFH in S1 unambiguously reveals how the inside-out growth of M33's inner disc (W09b) extends all the way to the disc edge. In comparison, the outer field, S2, is older (mean age $\sim 7 \pm 2$ Gyr), more metal-poor (mean $[M/H] \sim -0.8 \pm 0.3$ dex) and contains ~ 30 times less stellar mass.

These results provide the most compelling evidence yet that M33's age gradient reverses at large radii near the break radius. As noted by W09b, this behaviour is generally consistent with the simulations of Roškar et al. (2008b), in which the inner disc forms inside-out and the region beyond the break is populated with stars that migrated from the inner disc. If this scenario is correct, the radial mixing could in principle contaminate the sample in S1 with stars that migrated from the inner disc. However, we argue that this effect is likely to be small given the small fraction of stars older than 4.5 Gyr in S1 ($\sim 14\%$) relative to the inner disc where such stars are common ($\gtrsim 50\%$).

There remain alternative explanations for the behaviour of M33's mean age profile that we cannot completely rule out. One explanation involves a drop in the SFR caused by a warping of the gas disc (Sánchez-Blázquez et al. 2009). Another involves a change in the SF efficiency, perhaps caused by the gas density dropping below a critical value or by the sharp drop in stellar mass at the break radius (Bigiel et al. 2008; Leroy et al. 2008). A third explanation involves a transition to another component with a different SFH than the inner disc, such as a halo, thick disc, or accreted substructure. Kinematic information for individual stars in S2 as well as a global comparison between the gas and stellar surface densities near the break radius would help distinguish between these different possibilities.

ACKNOWLEDGMENTS

We thank David Thilker for sharing his HI data with us, Edouard Bernard for helpful advice about variable stars, Sebastian Hidalgo for useful discussions on the CMD fitting, and the anonymous referee whose feedback helped

improve the content of this paper. The optical image of M33's inner disc in Fig. 1 is provided courtesy of T.A.Rector (NRAO/AUI/NSF and NOAO/AURA/NSF) and M.Hanna (NOAO/AURA/NSF). This paper is based on observations made with the NASA/ESA Hubble Space Telescope, obtained at the Space Telescope Science Institute, which is operated by the Association of Universities for Research in Astronomy, Inc., under NASA contract NAS 5-26555. These observations are associated with program GO-9837. This work has made use of the IAC-STAR Synthetic CMD computation code. IAC-STAR is supported and maintained by the computer division of the Instituto de Astrofísica de Canarias. This work has made use of the resources provided by the Edinburgh Compute and Data Facility (ECDF; <http://www.ecdf.ed.ac.uk/>). The ECDF is partially supported by the eDIKT initiative (<http://www.edikt.org.uk>).

REFERENCES

- Abadi M. G., Navarro J. F., Steinmetz M., Eke V. R., 2003, *ApJ*, 597, 21
- Aparicio A., Gallart C., 2004, *AJ*, 128, 1465
- Aparicio A., Gallart C., Bertelli G., 1997, *AJ*, 114, 680
- Aparicio A., Hidalgo S. L., 2009, *AJ*, 138, 558
- Asplund M., Grevesse N., Sauval A. J., Scott P., 2009, *ARA&A*, 47, 481
- Barker M. K., Sarajedini A., Geisler D., Harding P., Schommer R., 2007, *AJ*, 133, 1138 (B07)
- Bernard E. J. et al., 2009, *ApJ*, 699, 1742
- Bertelli G., Mateo M., Chiosi C., Bressan A., 1992, *ApJ*, 388, 400
- Bigiel F., Leroy A., Walter F., Brinks E., de Blok W. J. G., Madore B., Thornley M. D., 2008, *AJ*, 136, 2846
- Blanton et al. M. R., 2003, *ApJ*, 594, 186
- Bothun G. D., 1992, *AJ*, 103, 104
- Bresolin F., Stasińska G., Vílchez J. M., Simon J. D., Rosolowsky E., 2010, *MNRAS*, 404, 1679
- Brook C. B., Kawata D., Gibson B. K., Freeman K. C., 2004, *ApJ*, 612, 894
- Brooks A. M., Governato F., Quinn T., Brook C. B., Wadsley J., 2009, *ApJ*, 694, 396
- Brown T. M., Ferguson H. C., Smith E., Kimble R. A., Sweigart A. V., Renzini A., Rich R. M., 2004, *AJ*, 127, 2738
- Brown T. M., Smith E., Ferguson H. C., Rich R. M., Guhathakurta P., Renzini A., Sweigart A. V., Kimble R. A., 2006, *ApJ*, 652, 323
- Burstein D., 1979, *ApJ*, 234, 829
- Charbonneau P., 1995, *ApJS*, 101, 309
- Chen Y. Q., Zhao G., Zhao J. K., 2009, *ApJ*, 702, 1336
- Cole A. A. et al., 2007, *ApJ*, 659, L17
- Corbelli E., Schneider S. E., 1997, *ApJ*, 479, 244
- Dalcanton J. J., Bernstein R. A., 2002, *AJ*, 124, 1328
- de Vaucouleurs G., de Vaucouleurs A., Corwin Jr. H. G., Buta R. J., Paturel G., Fouque P., 1991, *Third Reference Catalogue of Bright Galaxies*, Vols 1–3. Springer-Verlag, Berlin, Heidelberg, New York, p. 7
- Dolphin A. E., 2000, *PASP*, 112, 1383
- Dolphin A. E., 2002, *MNRAS*, 332, 91
- Dotter A. et al., 2010, *ApJ*, 708, 698
- Dunkley J. et al., 2009, *ApJS*, 180, 306

- Elmegreen B. G., Parravano A., 1994, *ApJ*, 435, L121
 Elston R., Silva D. R., 1992, *AJ*, 104, 1360
 Fall S. M., Efstathiou G., 1980, *MNRAS*, 193, 189
 Ferguson A., Irwin M., Chapman S., Iбата R., Lewis G., Tanvir N., 2007, in de Jong R. S., ed., *Island Universes: Structure and Evolution of Disk Galaxies*. Springer-Verlag, Dordrecht, p. 239
 Ferguson A. M. N., Wyse R. F. G., Gallagher J. S., Hunter D. A., 1998, *ApJ*, 506, L19
 Gallagher J. S. e. a., 1996, *ApJ*, 466, 732
 Gallart C., Freedman W. L., Aparicio A., Bertelli G., Chiosi C., 1999, *AJ*, 118, 2245
 Gallart C., Zoccali M., Aparicio A., 2005, *ARA&A*, 43, 387
 Galletti S., Bellazzini M., Ferraro F. R., 2004, *A&A*, 423, 925
 Gilmore G., Wyse R. F. G., Jones J. B., 1995, *AJ*, 109, 1095
 Girardi L., Bressan A., Bertelli G., Chiosi C., 2000, *A&AS*, 141, 371
 Girardi L., Salaris M., 2001, *MNRAS*, 323, 109
 Governato F. et al., 2009, *MNRAS*, 398, 312
 Grevesse N., Sauval A. J., 1998, *Space Sci. Rev.*, 85, 161
 Guidoni U., Messi R., Natali G., 1981, *A&A*, 96, 215
 Harris J., Zaritsky D., 2001, *ApJS*, 136, 25
 Harris J., Zaritsky D., 2004, *AJ*, 127, 1531
 Hernandez X., Gilmore G., Valls-Gabaud D., 2000, *MNRAS*, 317, 831
 Holtzman J. A. et al., 1999, *AJ*, 118, 2262
 Kautsch S. J., 2009, *PASP*, 121, 1297
 Krauss L. M., Chaboyer B., 2003, *Sci*, 299, 65
 Kroupa P., 2002, *Sci*, 295, 82
 Layden A. C., 1998, *AJ*, 115, 193
 Layden A. C., Sarajedini A., 2000, *AJ*, 119, 1760
 Leroy A. K., Walter F., Brinks E., Bigiel F., de Blok W. J. G., Madore B., Thornley M. D., 2008, *AJ*, 136, 2782
 Martin C. L., Kennicutt Jr. R. C., 2001, *ApJ*, 555, 301
 Martínez-Delgado D., Aparicio A., Gallart C., 1999, *AJ*, 118, 2229
 Martínez-Serrano F. J., Serna A., Doménech-Moral M., Domínguez-Tenreiro R., 2009, *ApJ*, 705, L133
 Mayer L., Governato F., Kaufmann T., 2008, *Advanced Sci. Lett.*, 1, 7
 McConnachie A. W. et al., 2009, *Nature*, 461, 66
 McConnachie A. W., Chapman S. C., Iбата R. A., Ferguson A. M. N., Irwin M. J., Lewis G. F., Tanvir N. R., Martin N., 2006, *ApJ*, 647, L25
 McLean I. S., Liu T., 1996, *ApJ*, 456, 499
 Minniti D., Olszewski E. W., Rieke M., 1993, *ApJ*, 410, L79
 Morrison H. L., Miller E. D., Harding P., Stinebring D. R., Boroson T. A., 1997, *AJ*, 113, 2061
 Neeser M. J., Sackett P. D., De Marchi G., Paresce F., 2002, *A&A*, 383, 472
 Okamoto T., Eke V. R., Frenk C. S., Jenkins A., 2005, *MNRAS*, 363, 1299
 Peebles P. J. E., 1984, *ApJ*, 277, 470
 Pietrinferni A., Cassisi S., Salaris M., Castelli F., 2004, *ApJ*, 612, 168
 Pohlen M., Trujillo I., 2006, *A&A*, 454, 759
 Riess A., Mack J., 2004, *ACS Instrument Science Report*, 2004-006
 Robertson B., Bullock J. S., Cox T. J., Di Matteo T., Hernquist L., Springel V., Yoshida N., 2006, *ApJ*, 645, 986
 Robin A. C., Reylé C., Derrière S., Picaud S., 2003, *A&A*, 409, 523
 Rogstad D. H., Wright M. C. H., Lockhart I. A., 1976, *ApJ*, 204, 703
 Roškar R., Debattista V. P., Quinn T. R., Stinson G. S., Wadsley J., 2008a, *ApJ*, 684, L79
 Roškar R., Debattista V. P., Stinson G. S., Quinn T. R., Kaufmann T., Wadsley J., 2008b, *ApJ*, 675, L65
 Sánchez-Blázquez P., Courty S., Gibson B. K., Brook C. B., 2009, *MNRAS*, 398, 591
 Sarajedini A., Barker M. K., Geisler D., Harding P., Schommer R., 2006, *AJ*, 132, 1361
 Sarajedini A., Geisler D., Schommer R., Harding P., 2000, *AJ*, 120, 2437
 Schaye J., 2004, *ApJ*, 609, 667
 Schlegel D. J., Finkbeiner D. P., Davis M., 1998, *ApJ*, 500, 525
 Sirianni M. et al., 2005, *PASP*, 117, 1049
 Skillman E. D., 1987, in Persson C. J. L., ed., *NASA Conf. Publ. Vol. 2466, Star Formation in Galaxies*. NASA, Washington, p. 263
 Sommer-Larsen J., Götz M., Portinari L., 2003, *ApJ*, 596, 47
 Steinmetz M., Navarro J. F., 2002, *New Astronomy*, 7, 155
 Stetson P. B., 1996, *PASP*, 108, 851
 Stewart K. R., Bullock J. S., Wechsler R. H., Maller A. H., 2009, *ApJ*, 702, 307
 Taylor C. L., Brinks E., Pogge R. W., Skillman E. D., 1994, *AJ*, 107, 971
 Thilker D. A., Braun R., Walterbos R. A. M., 2002, in Taylor A.R., Landecker T.L., Willis, A.G., eds, *ASP Conf. Ser. Vol. 276, Seeing Through the Dust: The Detection of HI and the Exploration of the ISM in Galaxies*. Astron. Soc. Pac., San Francisco, p. 370
 Tolstoy E., Saha A., 1996, *ApJ*, 462, 672
 Tosi M., Greggio L., Marconi G., Focardi P., 1991, *AJ*, 102, 951
 U V., Urbaneja M. A., Kudritzki R., Jacobs B. A., Bresolin F., Przybilla N., 2009, *ApJ*, 704, 1120
 van den Bosch F. C., 2001, *MNRAS*, 327, 1334
 van der Kruit P. C., 1987, *A&A*, 173, 59
 White S. D. M., Rees M. J., 1978, *MNRAS*, 183, 341
 Williams B. F., Dalcanton J. J., Dolphin A. E., Holtzman J., Sarajedini A., 2009b, *ApJ*, 695, L15 (W09b)
 Williams B. F. et al., 2009a, *AJ*, 137, 419
 Yoachim P., Dalcanton J. J., 2008, *ApJ*, 683, 707

This paper has been typeset from a $\text{\TeX}/\text{\LaTeX}$ file prepared by the author.